Proceedings of the 6th International Conference on Materials Chemistry and Environmental Engineering
DOI: 10.54254/2755-2721/2026.KA31247

Flow Mechanisms and Aerodynamic Optimization of Dual-Element Rear Wings via Orthogonal Design of Experiments, Computational Fluid Dynamics, and Wind Tunnel Testing

Xiaoke Yu

Milton Academy, Milton, USA
Collins.x.yu@gmail.com

Abstract. Rear wings play a critical role in Formula 1 race cars by generating a large proportion of the total aerodynamic downforce, and this study examines the aerodynamics of a dual-element rear wing within a Formula 1 framework using a combined methodology that includes theoretical analysis, computational fluid dynamics (CFD), design of experiments (DoE), and wind-tunnel testing. A two-stage Taguchi approach is employed to efficiently identify and optimize key geometric parameters with the aim of improving the lift-to-drag ratio while maintaining sufficient downforce. The theoretical analysis provides a physical basis for interpreting the behavior of multi-element wing systems, while CFD results show that the optimized configuration achieves improved aerodynamic efficiency through balanced pressure recovery, controlled boundary-layer development, and reduced vortex-induced losses. Wind-tunnel experiments are used to validate the numerical predictions, and a close agreement in lift-to-drag ratio is observed despite differences in Reynolds number. Overall, the results indicate that the flap element angle of attack is the dominant factor affecting aerodynamic efficiency, whereas camber distribution mainly controls the trade-off between downforce and drag, with a moderate camber of approximately 4% offering the most favorable compromise. Flow-field analyses link superior performance to favorable pressure recovery, reduced viscous dissipation, and controlled vortex dynamics, while experiments highlight the sensitivity of dual-element wings to off-design angles of attack. In the end, through numerous optimization steps, this study produced a package of four rear wing profiles, all with a downforce-to-drag ratio above 10, with the best case having a ratio of 11.88. On top of the high efficiency, these rear wing profiles alone produced at least 564.68 Newtons and up to 816.91 Newtons of downforce at a Reynolds number of around 1.2×10^6 . The success in optimizing aerodynamic efficiency while generating substantial downforce verifies the viability and efficacy of the methods presented in this study. Future work should explore other potential factors impacting dual-element rear wing performance, including different camber and thickness parameters, concavity control, and gurneys, to develop a more comprehensive aerodynamic performance map.

Keywords: dual-element rear wing, Taguchi method, computational fluid dynamics (CFD), bench-top wind tunnel, lift-to-drag ratio, downforce

DOI: 10.54254/2755-2721/2026.KA31247

1. Introduction

1.1. Background and current research

Formula 1 is the fastest circuit racing series on Earth [1]. The single-seater, open-wheel race cars in Formula 1 clock lap times and break records constantly, and these vehicles, armed with aerodynamics packages, speed around not just straights, but also corners at more than 300 km/h [2,3]. The incredible aerodynamics performance glue these cars to the ground and allows drivers to race under extreme g-forces.

Figure 1. Formula 1 car racing on track (CC0 public domain, sourced from Public Domain Pictures.net) [4]

Enhancing the aerodynamic efficiency of these race cars relies on two principal objectives: reducing drag and increasing downforce. Enhancing the aerodynamic efficiency of race cars relies on two principal objectives: reducing drag and increasing downforce. Devices such as spoilers, diffusers, and multi-element wings are therefore widely employed to regulate airflow, improve stability, and optimize performance. Among these, the rear wing is particularly critical in Formula 1, as it must simultaneously deliver high downforce in cornering while limiting drag on straights.

Modern rear wings are usually designed as multi-element systems, consisting of a main plane together with one or more flap elements. The flow passing through the slot between these elements interacts with the main plane and helps re-energize the boundary layer, which in turn increases suction and delays stall. In practice, however, the aerodynamic performance of such configurations is highly sensitive to geometric details. Even small changes in flap–main overlap, gap size, or relative incidence can noticeably alter wake structures, separation behavior, and the onset of stall [5]. Experiments performed under moving-ground conditions further indicate that variations in ride height can introduce wall-jet instabilities and intensify tip-vortex formation, leading to strongly nonlinear aerodynamic responses [6]. A similar sensitivity is observed under yawed inflow conditions that are representative of cornering, where both CFD simulations and wind-tunnel tests show that rear wings tend to experience asymmetric loading and a reduction in downforce unless the airfoil profiles and endplate geometries are considered together during optimization [7]. In addition, geometric parameters such as endplate clearance and endplate height also influence induced drag and vortex trajectories, although in many optimization frameworks these parameters are often treated as fixed rather than actively explored [8].

DOI: 10.54254/2755-2721/2026.KA31247

Recent work has explored active devices. Monteiro [9] investigated the Drag Reduction System (DRS) on a Formula Student vehicle, showing that adjusting the angles of attack of rear-wing elements can yield up to 94.5% drag reduction when flap angles and rotation points are tuned. This illustrates the effectiveness of flap-angle tailoring in exploiting wake interactions and demonstrates its value as an optimization strategy. Other studies have examined gap and overlap optimization [5], DRS configurations [10], and validation of aerodynamic predictions using the NASA 30P30N benchmark dataset [11]. While these contributions are significant, most assume fixed airfoil profiles for the main and flap elements, and focus exclusively on positional tuning. Such approaches overlook profile-dependent characteristics—camber, thickness distribution, suction-peak intensity, and pressure recovery—that directly affect stall behavior and transition sensitivity, particularly in inverted, ground-effect conditions.

Although multi-parameter optimization methods (e.g. Taguchi design, gradient-based approaches, surrogate modeling) have been successfully applied to aerodynamic design in other contexts, their use in co-optimizing both airfoil profile and rigging geometry for Formula 1 rear wings remains limited. Furthermore, combined CFD and experimental validation of such optimization strategies is rare.

1.2. Formula 1 regulations

The scope of aerodynamics optimization in this study adheres strictly to the FIA technical regulations. According to the 2025 ruleset, the rear wing assembly comprises several components: Rear Wing Profiles, Pylon, Rear Wing Beam, Rear Wing Endplate Body, Rear Wing Tip, and Rear Wing Separators. This study focuses exclusively on the Rear Wing Profiles, as they exert the dominant influence on aerodynamic performance.

The profiles must satisfy all geometrical requirements. The flap chord must be shorter than that of the main element, and when viewed in the XZ plane both profiles must fit entirely within the FIA-defined reference volume (RV-RW-PROFILES), illustrated in Fig. 2. In addition, the concave radius of curvature of all sections must exceed 100 mm, and the assembly must be symmetric about the vehicle centerline, with a maximum permitted half-span of 480 mm. Since this study isolates the influence of the profiles, their relative position to other components is neglected, with only the reference-volume constraints enforced.

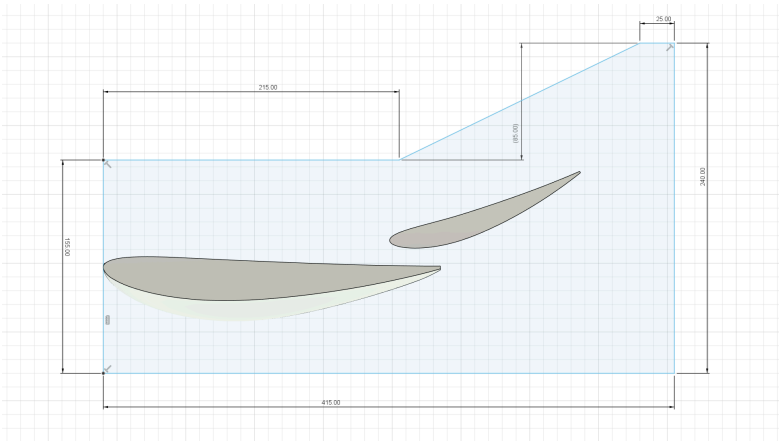

Figure 2. Schematic of the largest permitted rear-wing design used in this study, positioned within the RV-RW-PROFILES reference volume (viewed in theXZplane)

DOI: 10.54254/2755-2721/2026.KA31247

1.3. The present work

This paper presents an integrated investigation into the aerodynamics of dual-element Formula 1 rear wings, combining analysis of FIA regulations, theoretical modeling, CFD, design of experiments (DoE), and experimental validation. The objective is to systematically identify optimal configurations that maximize lift-to-drag ratio while ensuring substantial downforce generation.

A two-stage Taguchi design-of-experiments (DoE) framework is employed. In the first stage, candidate airfoil families with different camber, thickness, and suction characteristics are screened for use on the main plane, outboard section, and flap element. In the second stage, camber distributions within the most promising profiles are further refined in order to improve the lift coefficient (C_L) and overall aerodynamic efficiency (L/D), while remaining compliant with FIA regulations on element gap and curvature. The resulting candidate geometries are assessed using CFD simulations, which are validated against wind-tunnel measurements performed at Reynolds numbers of approximately $1–2 \times 10^6$ under ground-effect conditions, thereby ensuring relevance to real operating environments.

By jointly optimizing airfoil shape and rigging geometry under realistic regulatory constraints, this work addresses a key shortcoming of prior studies and establishes a systematic, experimentally validated framework for multi-element wing design. The remainder of the paper is organized as follows: Section 2 describes the orthogonal DoE methodology, CFD simulations, and wind-tunnel setup. Section 3 presents results and discussion, while Section 3 summarizes conclusions and outlines future research directions.

2. Methodology

2.1. Orthogonal design of experiments

The aerodynamic performance of a Formula 1 dual-element rear wing is dictated by a complex interplay of geometric parameters that jointly influence downforce and drag. Given the high dimensionality of this design space, a full factorial exploration would be computationally prohibitive. To address this challenge, a first-stage Design of Experiments (DoE) was carried out using a two-factor L8 orthogonal array. This approach allows systematic evaluation of seven key geometric parameters with only eight computational cases, significantly reducing the computational burden while retaining statistical robustness.

The selected factors, summarized in Table 1, include: the main-element chord length (C_1), flap-element chord length (C_2), three airfoil profile assignments (A_1 , A_2 , A_3), flap-element angle of attack (Ang.), and the vertical inter-element gap (Gap). Each parameter was varied at two levels—minimum and maximum—consistent with realistic Formula 1 design ranges. The resulting eight rear-wing geometries cover a representative portion of the feasible design space.

For the chord parameters, C_1 was varied between 250 mm and 225 mm, while C_2 ranged from 150 mm to 125 mm, yielding a typical flap-to-main chord ratio of about 0.5. Both elements were constrained to remain within the reference surface shown in Fig. 2.

The main element's edge airfoil profile, A_1 , alternated between the NACA 4412 and NACA 6412. The NACA 4412 provides high lift-to-drag performance at $Re \sim 10^6$ and exhibits relatively high stall angles, a desirable trait for tip regions prone to separation [12], [13,14]. The NACA 6412, with 6% maximum camber compared to the 4412's 4%, also performs efficiently at similar Reynolds numbers and promotes smooth pressure recovery, mitigating vortex formation near the tips [15,16].

DOI: 10.54254/2755-2721/2026.KA31247

For the flap element airfoil, A_2, the NACA 6412 was compared against the S1223. The NACA 6412 was chosen for its smooth pressure recovery, which is critical since the flap operates in the wake of the main element and is sensitive to separation onset [15,16]. The S1223, featuring 8.1% camber at 49% chord and an aggressive suction-side trailing edge, has proven efficient at lower Reynolds numbers ($Re \sim 2 \times 10^5$) [17,18]. Given the shorter flap chord, the effective Reynolds number is indeed lower than that of the main element, making the S1223 a promising candidate.

The central main-element profile, A_3, was set as either the NACA 6412 or E423. The NACA 6412 provided consistency checks against its use at the tips, while the E423, with its higher 9.5% camber, offers stronger suction peaks and thus greater lift [19-21]. Such high-camber sections are generally avoided near tips, where susceptibility to three-dimensional separation is higher, but can be effectively employed at mid-span where loading is typically greater [22,23]. A schematic of all employed airfoil profiles is shown in Fig. 3.

The flap relative angle (Ang.) was varied between 10° and 20°. Defined as the angle between the chord lines of the main and flap elements, this parameter effectively represents their relative incidence. Moderate values were chosen, as the main element already operates at a positive incidence relative to the freestream; setting the flap at excessively high angles risks early stall due to the combined effective angle of attack [24]. Finally, the inter-element gap was set at 9.5 mm and 12.9 mm. These levels correspond to Formula 1 regulations of 9.4 mm and 13.0 mm, with an added 0.1 mm manufacturing tolerance.

With this parameterization, the DoE was able to examine a range of geometries that are consistent with regulatory constraints while still reflecting realistic aerodynamic trade-offs.

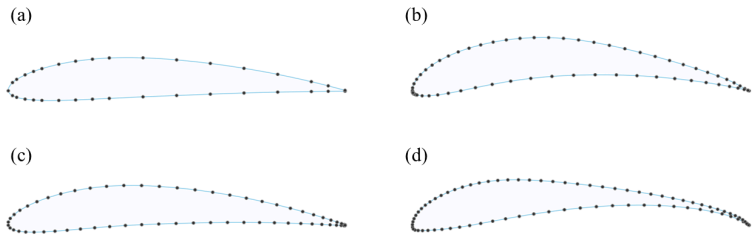

Figure 3. The four airfoil profiles used in this study. (a) corresponds to the NACA 4412, (b) corresponds to the E423, (c) corresponds to the NACA 6412, and (d) corresponds to the S1223

Based on the outcomes of the first-stage screening, a second-stage Taguchi design-of-experiments was carried out to further restrict the design space. In this stage, the focus was placed on identifying a parameter combination that leads to a higher lift-to-drag ratio (L/D), which is commonly used as an indicator of aerodynamic efficiency. By adopting an orthogonal array, the influence of individual factors can be separated more clearly, making it possible to assess their relative importance and to gain insight into the flow mechanisms that control the performance of dual-element rear wings.

DOI: 10.54254/2755-2721/2026.KA31247

Table 1. L8 orthogonal array experimental design for dual-element rear wing investigation

Case	C1	C2	Main Profile	Flap Profile	Add. Element	Angle	Gap
	(mm)	(mm)	(A1)	(A2)	(A3)	(deg)	(mm)
F1	245.0	122.5	NACA 4412	NACA 6412	NACA 6412	10	9.5
F2	245.0	122.5	NACA 4412	S1223	E423	20	12.9
F3	245.0	147.0	NACA 6412	NACA 6412	NACA 6412	10	12.9
F4	245.0	147.0	NACA 6412	S1223	E423	20	9.5
F5	220.5	122.5	NACA 4412	NACA 6412	E423	20	12.9
F6	220.5	122.5	NACA 4412	S1223	NACA 6412	20	9.5
F7	220.5	147.0	NACA 6412	NACA 6412	E423	10	9.5
F8	220.5	147.0	NACA 6412	S1223	NACA 6412	10	12.9

2.2. Computational Fluid Dynamics (CFD)

2.2.1. Governing equations and turbulence modeling

The fundamental physics of fluid flow are governed by the Navier-Stokes equations. For an incompressible flow, these consist of the continuity equation, which represents mass conservation, and the momentum equations, which represent Newton's second law applied to a fluid.

The continuity equation ensures that mass is neither created nor destroyed:

$$\nabla \cdot \overrightarrow{u} = 0 \tag{1}$$

The momentum equations describe how the velocity field changes under the influence of forces:

$$\frac{\partial \overrightarrow{u}}{\partial t} + \left(\overrightarrow{u} \cdot \nabla\right)\overrightarrow{u} = -\frac{1}{\rho}\nabla p + \nu \nabla^2 \overrightarrow{u} \tag{2}$$

where $\overrightarrow{u}$ is the instantaneous velocity vector, p is the instantaneous pressure, ρ is the constant fluid density, and ν is the kinematic viscosity. The term $\left(\overrightarrow{u} \cdot \nabla\right)\overrightarrow{u}$ is the convective acceleration, $-\frac{1}{\rho}\nabla p$ is the pressure gradient force per unit mass, and $\nu \nabla^2 \overrightarrow{u}$ represents the diffusion of momentum due to viscous forces.

However, directly solving these equations for turbulent flows at high speeds (like those around a race car wing) is extremely computationally expensive because it requires resolving all turbulent motions, from the largest to the smallest scales. To make the problem tractable, the Reynolds-Averaged Navier-Stokes (RANS) approach is used. This method decomposes the flow variables into a time-averaged mean and a fluctuating component:

$$\begin{aligned} ,\overrightarrow{u} &= \overrightarrow{U} + \overrightarrow{u} \\ p &= P + p' \end{aligned} \tag{3}$$

DOI: 10.54254/2755-2721/2026.KA31247

where $\overrightarrow{U}$ and P are the time-averaged velocity and pressure, and $\overrightarrow{u'}$ and p' are the turbulent fluctuations.

Substituting these decomposed variables into the momentum equation (2) and applying time-averaging (the Reynolds average) yields the RANS equations:

$$\frac{\partial \overrightarrow{U}}{\partial t} + \nabla \cdot \left(\overrightarrow{U} \otimes \overrightarrow{U} \right) = -\frac{1}{\rho} \nabla P + \nu \nabla^2 \overrightarrow{U} + \frac{1}{\rho} \nabla \cdot \left(-\rho \overline{\overrightarrow{u'} \otimes \overrightarrow{u'}} \right) \tag{4}$$

The term $-\rho \overline{\overrightarrow{u'} \otimes \overrightarrow{u'}}$ is the Reynolds stress tensor, denoted by τ_R. It represents the additional momentum transport due to turbulent fluctuations and introduces new unknowns, creating a "closure problem." To close this system of equations, a turbulence model is required.

The standard k - ε model, used in this study, is a two-equation eddy viscosity model. It proposes that the Reynolds stresses are proportional to the mean strain rate, analogous to viscous stresses:

$$\tau_R = 2\nu_t \overrightarrow{S} - \frac{2}{3} k \overrightarrow{I} \tag{5}$$

where ν_t is the turbulent (or eddy) viscosity, $\overrightarrow{S}$ is the mean strain rate tensor, k is the turbulent kinetic energy, and $\overrightarrow{I}$ is the identity tensor.

The model calculates ν_t by solving two additional transport equations. The first is for the turbulent kinetic energy k, which is the variance of the velocity fluctuations:

$$\frac{\partial k}{\partial t} + \nabla \cdot \left(k \overrightarrow{U} \right) = \nabla \cdot \left[\left(\nu + \frac{\nu_t}{\sigma_k} \right) \nabla k \right] + P_k - \varepsilon \tag{6}$$

Here, P_k is the production of turbulent kinetic energy by the mean flow, and ε is its dissipation rate.

The second equation is for the dissipation rate ε, which determines the scale at which turbulence energy is converted to heat:

$$\frac{\partial \varepsilon}{\partial t} + \nabla \cdot \left(\varepsilon \overrightarrow{U} \right) = \nabla \cdot \left[\left(\nu + \frac{\nu_t}{\sigma_\varepsilon} \right) \nabla \varepsilon \right] + C_{1\varepsilon} \frac{\varepsilon}{k} P_k - C_{2\varepsilon} \frac{\varepsilon^2}{k} \tag{7}$$

The turbulent viscosity is then computed as $\nu_t = C_\mu \frac{k^2}{\varepsilon}$. The model constants, determined from extensive experimental data for fundamental turbulent flows, are:

$$\begin{gathered} C_\mu = 0.09, \quad C_{1\varepsilon} = 1.44, \quad C_{2\varepsilon} = 1.92, \\ \sigma_k = 1.0, \quad \sigma_\varepsilon = 1.3. \end{gathered} \tag{8}$$

This closed set of equations allows for the prediction of the time-averaged flow around the rear wing, providing an efficient solution for engineering analysis.

DOI: 10.54254/2755-2721/2026.KA31247

2.2.2. Geometric modeling

The rear-wing elements were modelled in Autodesk Fusion 360 using airfoil coordinate data in Selig format obtained from airfoiltools.com. These coordinates were imported into Fusion via the Airfoil DAT to Spline add-in and projected onto the Y -plane. To reproduce the characteristic concave curvature of modern Formula 1 rear wings, two distinct profiles were employed for the main element: one located at the centerline and the other at the tip. The tip section was offset by 480 mm from the centerline to span the full permitted half-span. The two sections were smoothly connected using the Loft command, with straight guide rails constraining the leading and trailing edges to ensure geometric consistency. The lofted half-span was then mirrored across the Y -plane to yield the complete symmetric main element.

The auxiliary flap was generated from a single Selig-format profile extruded to a span of 960 mm. Its incidence relative to the main element was specified by rotation about the quarter-chord axis. Following this rotation, the flap was horizontally aligned such that its point of maximum camber coincided with the trailing edge of the main element, and then shifted aft by 20 mm to avoid potential negative effects brought by the flap element's overly forward position, such as wake bursting, boundary layer separation, weak pressure recovery, and stronger shock strength [25-27]. The vertical offset was adjusted until the minimum clearance between the elements matched the prescribed slot-gap specification.

During the second stage of the Taguchi-based refinement, the optimization of the rear-wing profiles was performed in a more constrained manner, with only the maximum camber of the selected airfoils being varied. For instance, the NACA 6412 profile, which originally has a maximum camber of 6%, was reduced to 4% in some configurations. This change was implemented by uniformly scaling the camber line. As a result, the thickness distribution, the position of the maximum camber, and the trailing-edge midline were kept unchanged, while only the slope and curvature of the camber line were modified.

Let a Selig-format airfoil be defined by coordinates $\{(x_i, y_i)\}_{i=0}^{N}$, ordered from trailing edge to leading edge along the suction surface and returning along the pressure surface. The leading-edge index is given by

$$i_{\mathrm{LE}} = \arg\min_{0 \le i \le N} x_i. \tag{9}$$

The upper and lower arcs are then represented by

$$(x_{u,j}, y_{u,j}) = (x_{i_{\mathrm{LE}}-j}, y_{i_{\mathrm{LE}}-j}), \quad j = 0, \ldots, i_{\mathrm{LE}}, \tag{10}$$

$$(x_{l,j}, y_{l,j}) = (x_{i_{\mathrm{LE}}+j}, y_{i_{\mathrm{LE}}+j}), \quad j = 0, \ldots, N - i_{\mathrm{LE}}. \tag{11}$$

Strict monotonicity in x is enforced through minimal perturbations if required. Linear interpolants for the upper and lower surfaces are defined as

$$y_u(x) = y_{u,j} + \frac{y_{u,j+1} - y_{u,j}}{x_{u,j+1} - x_{u,j}} (x - x_{u,j}), \tag{12}$$

with an analogous expression for $y_l(x)$.

The camber line and half-thickness distribution are then

DOI: 10.54254/2755-2721/2026.KA31247

$$y_c(x) = 1/2\,[y_u(x) + y_l(x)], \qquad y_t(x) = 1/2\,[y_u(x) - y_l(x)]. \tag{13}$$

The maximum camber $y_{c,\max}$ occurs at $x_{\max}$, i.e.

$$y_{c,\max} = \max_{x\in[0,1]} y_c(x). \tag{14}$$

To enforce a target camber m_{target}, the scaling factor

$$k = \frac{m_{\text{target}}}{y_{c,\max}} \tag{15}$$

is applied, giving a modified camber line $y_c'(x) = k\,y_c(x)$. The updated surfaces are reconstructed while preserving thickness:

$$y_u'(x) = y_c'(x) + y_t(x), \qquad y_l'(x) = y_c'(x) - y_t(x). \tag{16}$$

The modified coordinates are finally resampled at the original x-stations and output in standard Selig format.

As an illustrative example, consider the chord-wise location $x = 0.40$, where $y_u = 0.060$ and $y_l = -0.015$. The camber and half-thickness are

$$y_c = 0.0225, \quad y_t = 0.0375. \tag{17}$$

For $y_{c,\max} = 0.060$ and $m_{\text{target}} = 0.040$, the scaling factor is $k = 2/3$, yielding

$$y_c' = 0.0150, \quad y_u' = 0.0525, \quad y_l' = -0.0225. \tag{18}$$

The thickness remains unchanged, $y_u' - y_l' = 0.075$.

2.2.3. Flow domain and boundary conditions

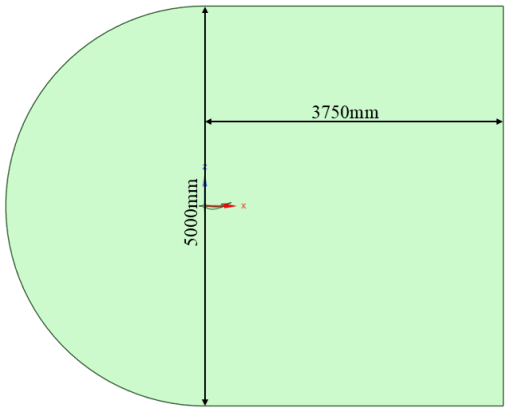

Figure 4. Schematic of the computational domain from the side

The computational domain was carefully designed to minimize boundary interference on the flow development around the wing assembly, as illustrated in Fig. 4. A right-handed Cartesian coordinate system was established with the streamwise direction along x, spanwise along y, and vertical along z, with the origin at the geometric center of the main element wing. All simulations were

DOI: 10.54254/2755-2721/2026.KA31247

conducted at zero angle of attack to isolate the effects of geometric variations from orientation. The domain extended $10L$ upstream, $15L$ downstream, and $5L$ in both lateral and vertical directions from the wing, where L denotes the largest possible chord length of the main element. A uniform velocity inlet of $U_\infty = 73\ m/s$ was prescribed in the x -direction, corresponding to a Reynolds number of 1.2×10^6 based on L . This inlet velocity is approximated from the 264.364 km/h average speed of the all-time fastest lap recorded around the Monza Circuit by a Formula 1 car [28]. The outlet was defined as a constant-pressure boundary, while the top and side boundaries were treated as slip walls. Wing surfaces were modeled as no-slip walls with enhanced wall functions to accurately resolve near-wall flow. Inlet turbulence intensity was set to 1% with a turbulence viscosity ratio of 10.

2.2.4. Aerodynamic force calculation

The wing assembly experiences aerodynamic forces due to the integrated effects of pressure and viscous shear stresses acting on its surfaces. These forces arise from the interaction between the wing geometry and the surrounding flow field, with pressure contributions normal to the surface and shear stresses tangential to it. To quantify these effects, the total aerodynamic forces were computed through surface integration of the pressure and shear stress distributions over all wing surfaces.

The resultant aerodynamic force was decomposed into drag and lift components in the streamwise and vertical directions, respectively. To assess the contribution of each wing element, surface force integrations were performed separately on the main element and on the flap. In this way, the aerodynamic behavior of the individual components, as well as their mutual interaction, can be examined, providing information on how the overall load is shared between the two elements in the multi-element arrangement. The surface integration followed a finite-volume formulation, with forces evaluated at each surface cell and then summed over the entire element. Pressure forces were obtained directly from the static pressure distribution, whereas viscous forces were derived from the wall shear stresses, maintaining consistency with the CFD solution and enabling reliable force evaluation.

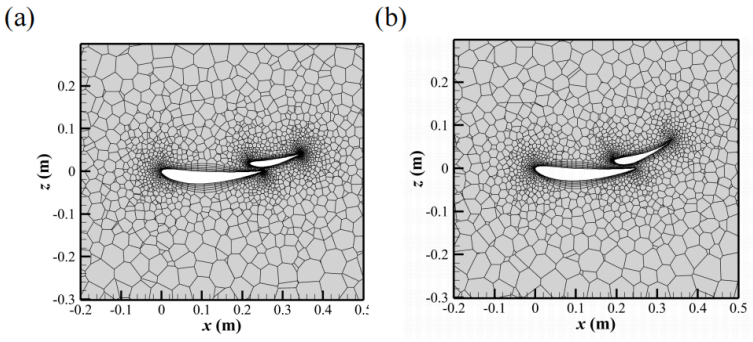

Figure 5. Two example illustrations of the mesh taken from their respective mid-plane slices

An unstructured mesh topology was applied throughout the computational domain, complemented by structured prismatic layers adjacent to all wing surfaces to resolve boundary-layer development accurately, as illustrated in Fig. 5. This hybrid meshing strategy combines the geometric flexibility of unstructured grids with the enhanced accuracy of structured layers in regions of critical flow. Near the wing surfaces, the mesh was refined with ten prism layers and a growth ratio of 1.2 to capture the viscous sublayer and log-law region effectively, while the first cell height

DOI: 10.54254/2755-2721/2026.KA31247

was carefully adjusted to maintain $y^+ < 1$ across all surfaces, ensuring proper representation of near-wall phenomena and accurate viscous force prediction. Three mesh resolutions were systematically evaluated for grid independence: coarse (570,000 cells), standard (970,000 cells), and fine (3 million cells). The study showed less than 0.5% variation in integrated lift and drag coefficients between the standard and fine meshes, as summarized in Table 2, while surface pressure distributions and flow separation characteristics exhibited negligible differences. Based on this assessment, the medium-resolution mesh was adopted for all subsequent simulations, providing a balanced compromise between computational efficiency and solution accuracy while maintaining engineering-level fidelity in both force prediction and flow-field resolution.

Table 2. Grid independence study comparing coarse, standard, and fine meshes

Mesh	Grid size (cells)	F_d (N)	F_l (N)	Rel. error F_d (%)	Rel. error F_l (%)
Coarse	570,000	81.06	-815.17	–	–
Standard	970,000	81.40	-816.91	0.41	0.21
Fine	3,000,000	81.17	-817.16	0.28	0.03

2.3. Wind tunnel experiments

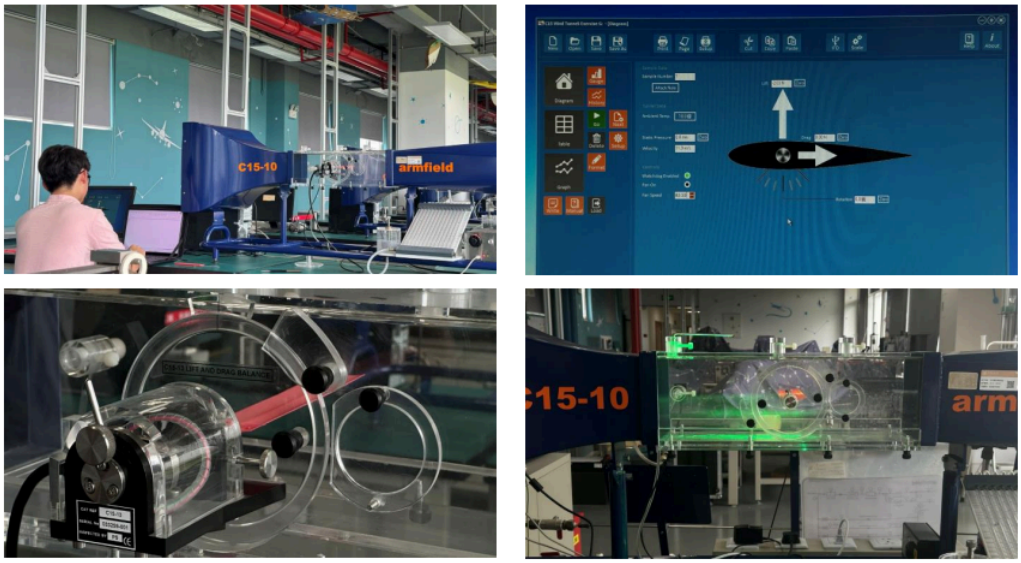

Figure 6. Armfield C15-10 Wind tunnel setup (top left). Armfield C15-10 Wind Tunnel software control (top right). 3D-printed rear wing model mounted on an Armfield C15-10 Wind Tunnel lift and drag balance module (bottom left). Armfield C15-10 Wind tunnel setup with a green laser beam shone from the bottom (bottom right)

DOI: 10.54254/2755-2721/2026.KA31247

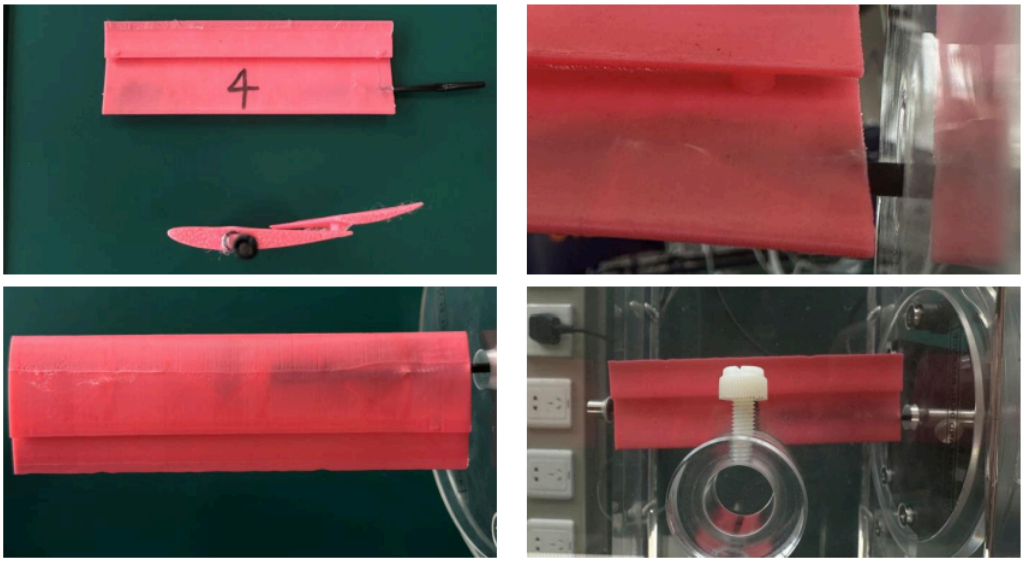

Figure 7. Side view and top view of the carbon fiber rod mounted into the side of the 3D-printed rear wing model (top left). Closeup view of the carbon fiber rod insertion of the 3D-printed rear wing model mounted on the lift and drag balance (top right). Bottom view of the 3D-printed rear wing model with the carbon fiber rod inserted (bottom left). Top view of the 3D-printed rear wing model mounted on the lift and drag balance in an Armfield C15-10 wind tunnel (bottom right)

Wind tunnel testing was conducted using the Armfield C15-10 Computer Controlled Subsonic Wind Tunnel, featuring a 9:4:1 contraction ratio and a maximum operational velocity of 34 m/s, as illustrated in Fig. 6. For the present investigation, the facility was operated at a maximum velocity of 15 m/s to maintain appropriate Reynolds number scaling, with the test section dimensions and flow quality characteristics detailed in Table 3.

One representative rear-wing configuration obtained from the computational study was selected for experimental validation. The model was manufactured using fused deposition modeling (FDM) with polylactic acid (PLA) material and was scaled to 0.15 of the original dimensions for force measurements (Fig. 5). In addition, a separate set of models with a scale of 0.13 was produced for flow visualization purposes. Each model was equipped with a precision-drilled mounting hole at the left tip of the main element, which was used to install a carbon-fiber support rod. This arrangement provided a stable connection to the force balance system while limiting aerodynamic interference, as illustrated in Fig. 7. Aerodynamic forces were measured using an integrated lift and drag balance with automatic data logging, and the system was calibrated in accordance with the manufacturer's specifications prior to testing. Flow velocity was obtained from the tunnel's built-in pressure-based measurement system and was regularly checked against a reference pitot-static probe. Before each experimental run, all measurement channels were zeroed to reduce systematic errors and to maintain measurement accuracy.

The experimental program examined five angles of attack (0°, 5°, 10°, 15°, and 20°) across six velocity conditions (15-90% of maximum velocity in 15% increments). The relative angle, defined as the angle between the main element chord line and the freestream direction, was verified using digital protractor measurements. For each test condition, data were acquired over a 30-second sampling period at 100 Hz to ensure statistical convergence of the force measurements.

DOI: 10.54254/2755-2721/2026.KA31247

Table 3. Wind tunnel test conditions and parameters

Parameter	Specification
Test section dimensions	300 mm × 300 mm × 600 mm
Maximum test velocity	15 m/s
Turbulence intensity	0.5%
Force balance resolution	0.01 N
Velocity measurement accuracy	± 1% of reading
Angle of attack range	0° to 20 °
Model scale (force measurements)	0.15
Model scale (flow visualization)	0.13
Data sampling rate	100 Hz

3. Results and discussion

3.1. Theoretical analysis of dual-element rear-wing aerodynamics

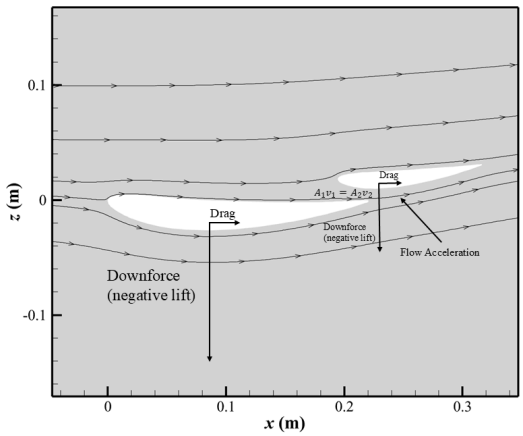

Figure 8. Schematic of aerodynamic forces and complex flow structures around a dual-element rear wing of an F1 car, including the formation of wingtip vortices and the turbulent wake

The dual-element rear wing on a Formula 1 car is not merely a downforce-generating device; it is the final and critical component in managing the car's overall aerodynamic flow structure. Its performance and interaction with downstream flow fields can be understood through fundamental fluid dynamic principles, which provide the theoretical basis for interpreting our experimental and computational results.

3.1.1. Downforce generation and pressure management

The primary function of the rear wing is to generate massive downforce, pressing the tires onto the track for superior cornering grip. This is achieved by creating a significant pressure difference between the upper and lower surfaces, as described by Bernoulli's principle for incompressible flow:

DOI: 10.54254/2755-2721/2026.KA31247

$$P + 1/2\rho v^2 = \text{constant}. \tag{19}$$

The highly cambered profiles of the main plane and flap are designed to accelerate the airflow over their upper surfaces, creating a low-pressure region (suction side), while the lower surface experiences relatively higher pressure. The resulting aerodynamic forces are quantified by:

$$L = C_L \cdot 1/2\rho U_\infty^2 S, \quad D = C_D \cdot 1/2\rho U_\infty^2 S, \tag{20}$$

where L is downforce (negative lift), D is drag, and S is the reference area. In F1, the efficiency metric is paramount:

$$\frac{L}{D} = \frac{C_L}{C_D}, \tag{21}$$

as it balances the need for cornering downforce against the straight-line speed penalty from drag.

3.1.2. The slot-gap effect and boundary layer control

The slot between the main element and the flap is a masterstroke of flow control. Acting as a nozzle, it accelerates the flow (as per the continuity equation, $A_1 v_1 = A_2 v_2$) and directs this high-energy jet onto the suction surface of the flap. This serves two vital purposes in the F1 context:

1. It energizes the boundary layer on the flap, enabling it to withstand the strong adverse pressure gradient ($\frac{dP}{dx} > 0$) without separating, thus allowing the flap to operate at high effective angles of attack.

2. It helps to seal the flow between the two elements, improving the pressure difference and maximizing downforce from both components.

3.1.3. Wake structures and their impact on overall car performance

The flow behind an F1 rear wing is highly complex and three-dimensional, dominated by powerful vortex structures (Figure 8).

• Wingtip Vortices: The pressure difference between the lower and upper surfaces causes air to curl around the wingtips, forming strong, coherent vortices. These structures are a major source of induced drag, quantified by:

$$C_{D_i} = \frac{C_L^2}{\pi AR \cdot e}. \tag{22}$$

• Turbulent Wake: The combined wake of the main element and flap is a region of low energy and high turbulence. This wake directly impacts the performance of downstream components. In modern F1 cars, the rear wing's wake interacts with the rear suspension elements and the diffuser's outflow. A disorganized wake can disrupt the diffuser's function, reducing its ground-effect downforce. Furthermore, this turbulent wake is a primary factor in the "dirty air" problem, significantly reducing the downforce of a following car and making overtaking difficult.

3.1.4. Interaction with the DRS and overall vehicle balance

The Drag Reduction System (DRS) is a pivotal application of this theory. By opening the slot gap and stalling the flap, DRS drastically reduces the flap's effective camber and lift coefficient C_L .

DOI: 10.54254/2755-2721/2026.KA31247

This achieves two simultaneous effects:

3. A significant reduction in overall drag D, allowing for higher straight-line speed.
4. A strategic redistribution of the car's aerodynamic balance (shift from rear downforce), which the driver must manage.

The design of the rear wing can therefore be regarded as a compromise. On the one hand, it is required to generate sufficient and efficient downforce for cornering performance. On the other hand, it should produce a wake that is relatively clean so as not to adversely affect following cars during overtaking, while also allowing the use of devices such as DRS to reduce drag when required. The need to balance downforce generation, drag reduction, and overall flow management helps explain why the rear wing has become one of the most intensively developed components in Formula 1.

3.2. Analysis of the first-stage screening DoE

3.2.1. Main effects analysis and factor ranking

The orthogonal experimental design was used to examine how airfoil geometry, camber distribution, and relative angle influence the aerodynamic performance of the multi-element airfoil system. From the main effects plots, it can be seen that the flap element angle of attack plays the dominant role in downforce generation, while changes in camber have a noticeable impact on both lift and drag behavior. The analysis of variance (ANOVA) shows that Factor A (airfoil type) and Factor B (flap element angle of attack) together explain more than 70% of the variation observed in the lift-to-drag ratio. In addition, interaction effects between flap angle of attack and camber are evident, suggesting that the aerodynamic response becomes strongly nonlinear, particularly at higher angles of attack.

Table 4. Taguchi L8 results with factor levels replaced by actual values. C1 = Main Chord. C2 = Auxiliary Chord. A1 = Main Airfoil Type. A2 = Auxiliary Airfoil Type. A3 = Main Airfoil Type 2. Ang. = Angle. l = Profile Gap. L/D = Lift/Drag

Case	C1	C2	A1	A2	A3	Ang.	l	Drag	Lift	L/D
1	245.00	122.50	NACA 4412	NACA 6412	NACA 6412	10.00	9.50	84.15	-846.29	-10.06
2	245.00	122.50	NACA 4412	S1223	E423	20.00	12.90	122.97	-1027.86	-8.36
3	245.00	147.00	NACA 6412	NACA 6412	NACA 6412	10.00	12.90	200.85	-1379.36	-6.87
4	245.00	147.00	NACA6412	S1223	E423	20.00	9.50	223.14	-1448.05	-6.49
5	220.50	122.50	NACA4412	NACA6412	E423	20.00	12.90	183.38	-1287.03	7.02
6	220.50	122.50	NACA4412	S1223	NACA 6412	20.00	9.50	174.60	-1277.45	7.32
7	220.50	147.00	NACA 6412	NACA 6412	E423	10.00	9.50	128.04	-1067.63	-8.34
8	220.50	147.00	NACA 6412	S1223	NACA 6412	10.00	12.90	94.40	-898.65	-9.52

DOI: 10.54254/2755-2721/2026.KA31247

Table 5. Taguchi analysis of $|C_l/C_d|$(L8 design)

	C1	C2	A1	A2	A3	Ang.	L
K_1	31.77	32.75	32.28	33.76	33.08	36.27	32.20
K_2	32.19	31.22	31.68	30.21	30.88	27.69	31.76
k_1	7.94	8.19	8.07	8.44	8.27	9.07	8.05
k_2	8.05	7.80	7.92	7.55	7.72	6.92	7.94
R	0.11	0.38	0.15	0.89	0.55	2.15	0.11

Ranking: Angle > A2 > A3 > C2 > A1 > L > C1. Optimum: C1 = 220.5, C2 = 122.5, A1 = NACA 4412, A2 = NACA 6412, A3 = NACA 6412, Ang. = 10, L = 9.5.

The Taguchi analysis indicates that the angle of attack of the flap element is the primary factor affecting the lift-to-drag ratio, with a range value (R) of 2.15, significantly exceeding that of other parameters. The camber of the auxiliary element (Ca2) ranks as the second most influential factor, emphasizing the importance of flap or slat camber in controlling pressure distribution and flow separation around the main airfoil. According to the response table, the optimal configuration corresponds to a moderate flap angle of 10°, combined with specific camber distributions and a reduced gap, achieving the maximum aerodynamic efficiency (|L/D|) under the tested conditions.

Table 6. Taguchi analysis of $|C_l/C_d|$(L8 design)

	C1	C2	A1	A2	A3	Ang.	L
K_1	31.77	32.75	32.28	33.76	33.08	36.27	32.20
K_2	32.19	31.22	31.68	30.21	30.88	27.69	31.76
k_1	7.94	8.19	8.07	8.44	8.27	9.07	8.05
k_2	8.05	7.80	7.92	7.55	7.72	6.92	7.94
R	0.11	0.38	0.15	0.89	0.55	2.15	0.11

Ranking: Angle > A2 > A3 > C2 > A1 > L > C1. Optimum: C1 = 220.5, C2 = 122.5, A1 = NACA 4412, A2 = NACA 6412, A3 = NACA 6412, Ang. = 10, L = 9.5.

3.2.2. Flow field analysis and physical mechanisms

Detailed computational fluid dynamics analyses were conducted to elucidate the physical mechanisms underlying the aerodynamic performance variations identified during the first-stage design of experiments. Investigation of the flow-field characteristics reveals a strong coupling between geometric configuration and aerodynamic response, illustrating how design modifications alter the surface pressure distribution and associated flow structures. Cases F1 and F4 were selected as representative examples, with Case 1 yielding a more favorable lift-to-drag ratio, while Case F4 produces higher downforce alongside significantly increased drag, which contributed to its comparatively lowest lift-to-drag ratio.

DOI: 10.54254/2755-2721/2026.KA31247

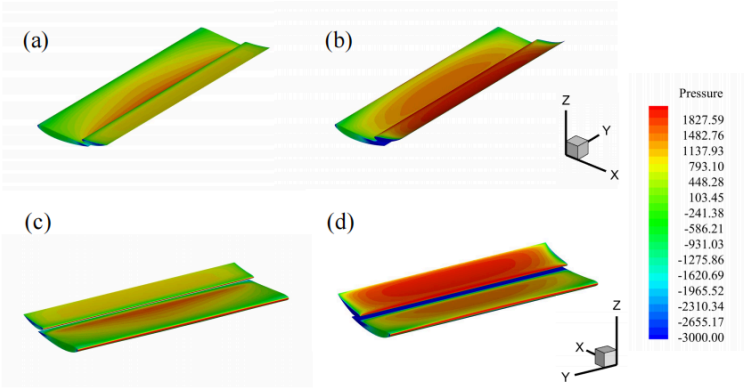

Figure 9. Three-dimensional surface pressure distribution over the dual-element rear wing for two representative configurations. Panels (a,c) correspond to Case F1 and panels (b,d) to Case F4, each shown from two different perspectives

The surface pressure distribution over the wing assembly, presented in Fig. 9, exhibits distinct patterns between these cases. As shown in Fig. 9, Case F1's main element's pressure peak is more concentrated towards the trailing edge while Case F4's main element pressure peak is more spread out towards the middle of the element. This locational difference of the pressure peak may be caused by F4's higher maximum central camber of 9.5 % governed by its E423 central airfoil whereas F1's maximum central camber is only 6% from its NACA 6412 design. The earlier pressure peak would also shift the stagnation point forwards thus starting pressure recovery earlier, and coupled with the effect of the higher camber, can contribute to a stronger adverse gradient and thus lead to more severe flow separation. Towards the horizontal ends of the main element, however, Case F1's lower maximum camber of 4% from the NACA 4412 airfoil and F4's 6% camber from its NACA 6412 airfoil did not produce a noticeable difference in the pressure peak. On the flap, Case F1 produces a more moderate pressure peak, resulting in a measured reduction in downforce but a significantly smaller drag increment. In contrast, Case F4 develops a stronger pressure peak, which enhances downforce but also leads to a substantial increase in drag. Another potential contributor to F4's higher downforce is the larger relative angle between the flap and the main element, which would cause a larger portion of the incoming airflow to act on the flap, resulting in higher downforce and drag. Case F4 also likely has a better slot-jet re-energization that adds momentum to the boundary layer as indicated by the stronger suction on the trailing edge of the main element and leading edge of the flap. This stronger suction would generate more downforce in comparison to the lack of such an effect in F1. Overall, Case F1 achieves a higher lift-to-drag ratio, indicating that it provides a more efficient balance between downforce and drag while Case F4's multiple design features produced a more downforce aggressive rear wing package.

DOI: 10.54254/2755-2721/2026.KA31247

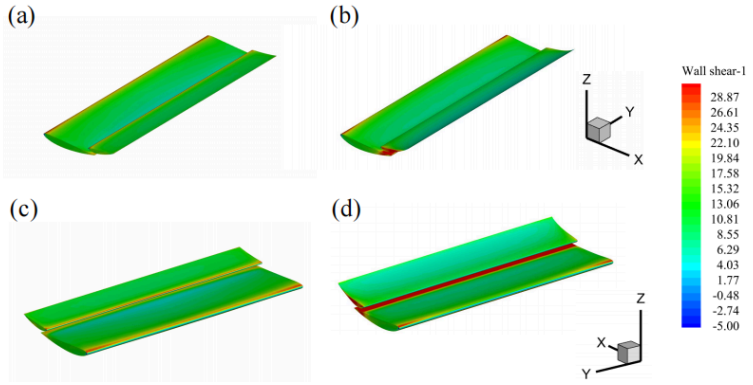

Figure 10. Three-dimensional streamwise wall shear stress distribution over the dual-element rear wing for two representative configurations. Panels (a,c) correspond to Case F1 and panels (b,d) to Case F4, each shown from two different perspectives

The streamwise wall-shear distribution presented in Fig.10 reveals clear differences in boundary-layer behavior between Cases F1 and F4, which correspond directly to the pressure-side loading shown in Fig.9. In Case F1, a distinct thin band of reduced wall shear appears near the trailing edge of the main element (Fig.10). This low-shear strip coincides with a region of elevated pressure in the same location on the pressure plot (Fig.9), indicating that the local flow may have undergone significant deceleration under an adverse pressure gradient. The attenuated wall-parallel velocity gradient implies a thickened, weakened boundary layer approaching separation. This behavior is consistent with the lower camber of the NACA 4412 main profile and the smaller 10° geometric angle, which limits momentum growth along the pressure side and produces a milder pressure-recovery process. As a result, Case F1 develops only moderate boundary-layer re-energization on its flap and maintains comparatively uniform, mid-range wall-shear levels over both elements, contributing to its lower magnitude of downforce and reduced drag, as also reflected by its higher lift-to-drag ratio but lower downforce in Table 4.

In contrast, Case F4 shows a noticeably different wall-shear pattern, which can be attributed to its more aggressive geometric configuration. The flap employs the S1223 profile with a maximum camber of 8.1% and operates at a larger angle of 20°. Under these conditions, an extended region of relatively high wall shear develops along the flap chord (Fig. 10), appearing as a pronounced red streak that indicates a high-momentum boundary layer sustained by a stronger slot-jet interaction between the main element and the flap. This behavior is consistent with the lower-pressure regions on the suction side and the increased pressure levels on the pressure side observed in Fig. 9, both of which contribute to higher circulation and aerodynamic loading. At the same time, a narrow light-blue region of low wall shear can be identified near the mid-chord of the flap. This region corresponds to a localized area of higher static pressure (Fig. 9) and reflects the presence of an adverse pressure gradient, suggesting local boundary-layer weakening or the formation of a small separation bubble despite the generally energetic flow. The combined effects of higher camber (E423 on the main element and S1223 on the flap), a longer auxiliary chord (C2 = 147 mm), and the increased flap angle lead to higher surface velocities over most of the flap and main element, which in turn raises streamwise shear and viscous drag. Taken together, these features explain the higher drag and increased downforce reported for Case F4 in Table 4, and consequently its lower aerodynamic efficiency relative to Case F1.

DOI: 10.54254/2755-2721/2026.KA31247

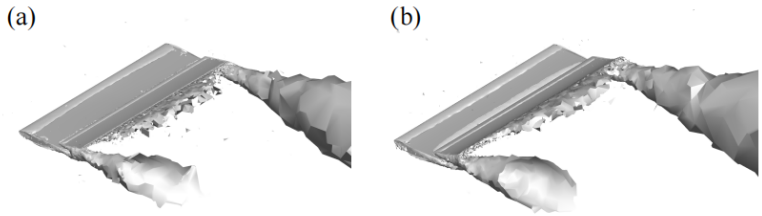

Figure 11. Vortical structures visualized using Q-criterion iso-surfaces:(a) Case F1, (b) Case F4

The Q-criterion iso-surfaces in Fig. 11 show only small differences between Cases F1 and F4. In both cases, the vortical structures have a similar topology, with comparable trailing-edge shear-layer roll-up and no major differences in vortex strength or coherence. This similarity may be related to the unchanged geometric features of the two configurations, including the thin trailing edges of the main element and flap, which produce the main shear layers, and the slot between elements, which allows the high-momentum jet to reattach to the flap in a similar manner. While Case F4 exhibits a slightly fuller wake downstream, which corresponds to its higher aerodynamic loading, the overall variations remain limited.

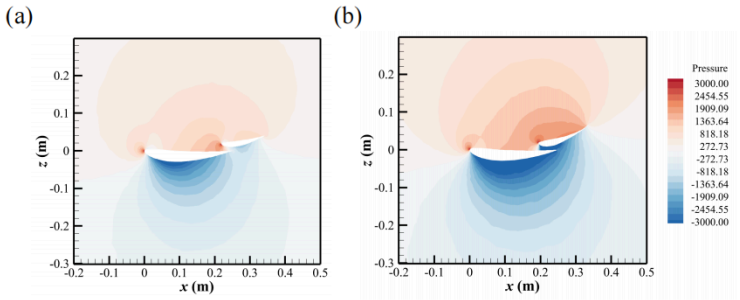

Figure 12. Static pressure contours in the mid-plane: (a) Case F1, (b) Case F4

The mid-plane pressure contour of Case F1 can be explained by the milder geometry of both its main element and flap element. On the main element, Case F1 employs the NACA 4412 and NACA 6412 airfoil profiles with maximum cambers of 4% and 6%, respectively (Table 4). These airfoils have lower maximum camber than their Case F4 counterparts, which limits the curvature of Case F1's streamlines, does not accelerate the airflow as much, and therefore limits the pressure difference between the pressure and suction side. The less-accelerated suction side airflow may cause the lower pressure region to not expand as far out as Case F4 does (Fig. 12). At the trailing edge of the main element, the pressure difference also remains modest because the 4412/6412 combination has a relatively gentle aft-loading distribution, so the downstream pressure contours remain compact. This behavior is consistent with the earlier observations of a small low-shear strip near the main trailing edge in Fig. 10, which indicated a mild adverse pressure gradient at the end of the main element.

On the flap, Case F1 uses a NACA 6412 profile, a comparatively short chord, and a flap angle of only 10° (Table 4). The 6% maximum camber of the NACA 6412 airfoil accelerates the re-energized airflow but does so less than the S1223 airfoil in Case F4; nonetheless, this acceleration resulted in the small pressure region under Case F1's flap. The 10° angle of the flap also did not drastically contribute to flow acceleration or achieve the effect of a higher camber rear wing as the angled flap's suction side followed the suction side upward curvature of the main element. The shorter C2 also shortens the distance over which the flap can develop pressure-side loading, contributing to

DOI: 10.54254/2755-2721/2026.KA31247

modest pressure gradients at its trailing edge. Combined, the front and rear geometries in F1 yield a pressure field with relatively small vertical extent and smaller overall pressure differences (Fig. 12), which is consistent with the lower lift and drag values in Table 4.

Case F4 shows different pressure magnitudes because both the front and rear geometries impose larger flow turning and stronger circulation. On the main element, the NACA 6412 and E423 airfoil profiles are used, the latter having distinctly higher camber than any main-element profile used in Case F1. This higher camber produces stronger streamline curvature, and thus a larger pressure difference around the main element. In Fig. 12 this appears as a broader and deeper low-pressure region under the main element of the wing. Additionally, higher camber toward the trailing edge of the main (E423) increases aft loading, which aligns with the stronger pressure and suction behind the main TE compared with Case F1. These main-element differences provide the initial increase in airflow circulation that is carried through the rest of the geometry.

On the flap, Case F4 differs from Case F1 in three aspects: a longer auxiliary chord (C2 = 147 mm), a higher-camber S1223 airfoil, and a larger flap angle of 20° (Table 4). These changes increase the pressure differences produced by the flap. The longer chord allows circulation to develop over a greater chordwise distance, while the higher camber of the S1223 section creates a larger suction region near the leading edge. In addition, the increased flap angle causes more pronounced flow turning. These effects can be seen in Fig. 12, where the low-pressure region beneath the flap extends more vertically and the high-pressure region above it is larger. The modified rear-element geometry also affects the slot jet. With the higher camber and flap incidence, the slot flow accelerates and the pressure behind the slot decreases more effectively, contributing to the downward expansion of the suction region under the flap.

This comprehensive flow analysis provides fundamental insights into how geometric parameters influence the aerodynamics of dual-element rear wings, rationalizing the performance trends observed in computational studies. The identified flow mechanisms and their connections with specific geometric changes and their aerodynamic consequences will be furthered in the next stage of the experimental process.

3.3. Analysis of the second-stage refinement DoE

3.3.1. Determination of optimal main factor values from the second-stage DoE

Table 7. Taguchi results (Angle, Ca2, Ca3) with factor levels replaced by actual values. L/D = l/d

Exp.	Angle(deg)	Ca2	Ca3	d(N)	l(N)	L/D
S1	6.00	6% Max Camber	4% Max Camber	55.13	-628.49	-11.40
S2	6.00	4% Max Camber	6% Max Camber	65.84	-709.05	-10.77
S3	10.00	6% Max Camber	6% Max Camber	81.40	-816.91	-10.04
S4	10.00	4% Max Camber	4% Max Camber	47.52	-564.68	-11.88

Building upon the findings of the first-stage DoE, which identified the flap element relative angle (Ang.), flap camber (Ca_2), and main element camber (Ca_3) as the primary influencing factors, a second-stage Taguchi experimental design was implemented for design refinement. This phase aimed to precisely determine the optimal combination of these parameters to maximize the lift-to-drag ratio (L/D), a critical metric for aerodynamic efficiency. The experimental layout and corresponding aerodynamic performance metrics are detailed in Table 6.

DOI: 10.54254/2755-2721/2026.KA31247

Analysis of the results confirms a strong interaction between the geometric parameters and the resultant forces. Configuration S4, with an Ang. of 10 °, a flap camber of 4% Max Camber, and a main element camber of 4% Max Camber, was identified as the optimal design. It achieved the highest L/D ratio of -11.88 by generating a substantial downforce (l) of −564.68 N with the lowest drag (d) of 47.52 N among all configurations. This result signifies the most favorable trade-off between downforce generation and drag penalty.

In contrast, configuration S3, which also has a flap angle of 10° but higher camber values (Ca2: 6% Max Camber, Ca3: 6% Camber), produced the largest downforce (−816.91 N) while experiencing a considerable increase in drag (81.40 N), resulting in the lowest lift-to-drag ratio of −10.04. This result reflects the trade-off between achieving high absolute downforce and maintaining aerodynamic efficiency. Configurations with a lower flap angle of 6°, namely S1 and S2, showed intermediate performance. Comparing these two cases further indicates that performance is sensitive to camber distribution, with S1 achieving a slightly better L/D (−11.40) than S2 (−10.77).

Based on the second-stage DoE, the optimal main factor values were determined as a flap angle of 10°, a flap camber (Ca2) of 4% maximum camber, and a main element camber (Ca3) of 4% maximum camber. This set of parameters can be used as a reference for achieving the highest aerodynamic efficiency (L/D) within the considered design space and offers guidance for the final design specification.

3.3.2. Optimal configurations and underlying flow mechanisms

The second-stage Design of Experiments (DoE) indicates that Case S4 is the configuration with the highest lift-to-drag ratio, resulting from a balanced combination of geometric parameters. An examination of the flow fields helps to explain the performance differences among the four configurations (S1–S4) and the fluid-dynamic factors affecting their aerodynamic behavior. This analysis considers the interactions between pressure drag, viscous drag, and flow separation, which together influence overall aerodynamic efficiency. Figure 13 shows the three-dimensional surface pressure distributions, where different patterns can be observed for each configuration. A key factor affecting performance is the management of adverse pressure gradients (APG), which directly influences flow separation and pressure drag. In Case S4, the pressure field appears well organized, with a strong suction peak on the main element and a moderate, evenly distributed low-pressure region on the flap, suggesting effective aerodynamic loading with limited flow separation and reasonably managed APGs. In comparison, Case S3 shows an intensified low-pressure region near the flap leading edge, resulting in higher downforce but also steeper adverse pressure gradients that may cause boundary-layer separation, increase pressure drag, and reduce aerodynamic efficiency.

The intermediate configurations S1 and S2 show transitional characteristics in their pressure distributions. In Case S2, the more concentrated low-pressure region on the main element suggests a higher effective camber, which is associated with increased downforce but lower aerodynamic efficiency compared to Case S1. The relationship between pressure distribution and geometric parameters implies that achieving good performance requires balancing suction intensity with gradual pressure recovery to reduce flow separation. In addition to the pressure analysis, Fig. 14 presents the streamwise wall shear stress distributions, providing information on boundary-layer development and viscous drag contributions. Wall shear stress (τ_w), which is proportional to the velocity gradient at the wall, indicates the state of the boundary layer and the level of frictional drag. Case S4 shows a relatively uniform shear stress distribution across both wing elements, suggesting attached flow and minimal viscous dissipation, which supports its higher efficiency. By contrast,

DOI: 10.54254/2755-2721/2026.KA31247

Case S3 exhibits extended regions of elevated shear stress, particularly on the main element, indicating thinner and more stressed boundary layers due to stronger adverse pressure gradients, which results in higher frictional drag and lower efficiency. Cases S1 and S2 have concentrated shear stress near the leading edges, reflecting sharp flow acceleration and thin boundary-layer formation. When combined with concentrated high-pressure regions near the gap, these characteristics correspond to effective flow turning through the slot region. Overall, the observed patterns indicate that leading-edge geometry plays an important role in managing boundary-layer development and limiting viscous drag.

The vortical structures shown in Fig. 15 illustrate three-dimensional flow behavior and induced drag characteristics. All configurations maintain coherent tip vortices, but differences are observed in vortex strength and secondary flow patterns. Cases S1, S2, and S4 develop stronger tip vortices, which generally correspond to higher lift and induced drag. In Case S3, although the downforce is the highest, the tip vortices are weaker. This may be due to the large low-pressure region on the flap causing flow separation in the inboard sections, which reduces loading on the wingtips and weakens the vortices. As a result, lift is generated less efficiently, with high downforce arising mainly from localized suction rather than uniform spanwise loading. Case S3 also shows small inboard vortices along the main element chord, indicating local boundary-layer separation, which produces unsteady low-pressure wakes that increase pressure drag without effectively contributing to downforce. In Case S4, these vortices are absent, suggesting better flow attachment and more efficient vortex formation. Figure 16 presents static pressure contours in the mid-plane, showing the slot-jet interaction between the wing elements and its effect on the wake. The slot-jet accelerates flow through the gap, injecting high-energy fluid into the main element's boundary layer. In Case S4, the pressure gradient across the slot region is clear, allowing smooth flow acceleration, which energizes the main element boundary layer, delays separation, and produces a narrower wake with higher base pressure, reducing pressure drag. In Case S3, a deep suction pocket appears at the flap leading edge followed by rapid pressure recovery, indicating that the slot flow accelerates excessively and then diffuses quickly, creating strong adverse gradients that trigger boundary-layer separation. The resulting wider wake and lower base pressure increase pressure drag, explaining the lower aerodynamic efficiency of S3 despite its high downforce.

The flow analysis provides several guidelines for multi-element wing design. Optimal configurations tend to manage adverse pressure gradients by balancing suction intensity with gradual pressure recovery, since steep adverse gradients can cause extensive separation that reduces overall efficiency even if local suction is increased. The gap and overlap between elements should be adjusted to achieve smooth flow acceleration through the slot, which energizes the main element boundary layer without causing excessive diffusion or separation on the flap. Maintaining attached flow over most of the wing surface appears more important than maximizing local suction peaks. Designs that reduce extreme local downforce in favor of better flow attachment usually achieve higher lift-to-drag ratios. Strong, coherent tip vortices are preferable to inboard separation-induced vortices, as the vortex structure reflects overall aerodynamic efficiency and spanwise loading. The superior performance of Case S4 is associated with its geometric combination—a 10° flap angle with 4% maximum camber on both elements—which maintains favorable pressure gradients, utilizes the slot-jet for boundary-layer control, limits viscous dissipation through attached flow, and avoids separation-induced vortices. This approach provides a framework for future multi-element wing design, showing that high aerodynamic efficiency depends on the integrated management of multiple flow mechanisms rather than the maximization of individual performance metrics.

DOI: 10.54254/2755-2721/2026.KA31247

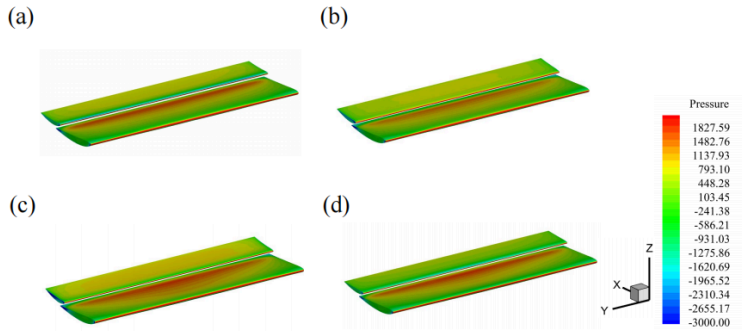

Figure 13. Three-dimensional surface pressure distribution over the dual-element rear wing configuration: (a) Case S1, (b) Case S2, (c) Case S3, and (d) Case S4. The balance between suction intensity and adverse pressure gradient management is critical for optimal performance

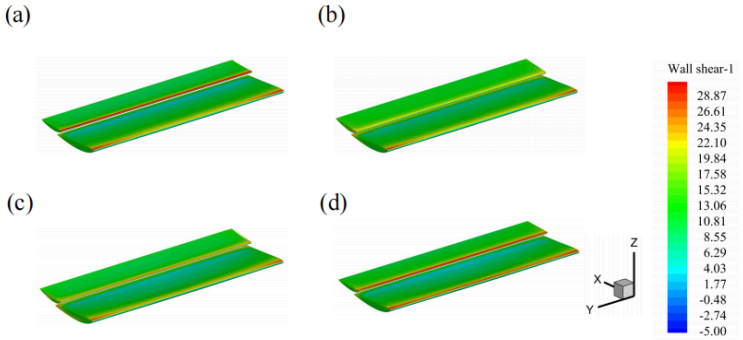

Figure 14. Three-dimensional streamwise wall shear stress distribution over the dual-element rear wing: (a) Case S1, (b) Case S2, (c) Case S3, and (d) Case S4. Wall shear stress distribution indicates boundary layer state and viscous drag contributions

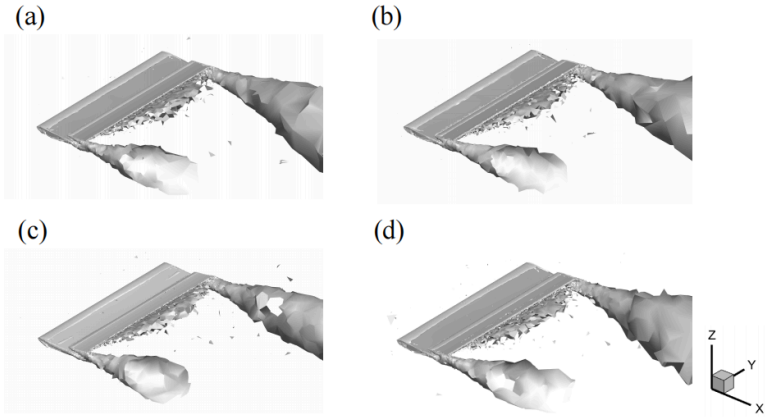

Figure 15. Vortical structures visualized using Q-criterion iso-surfaces: (a) Case S1, (b) Case S2, (c) Case S3, and (d) Case S4. Vortex structures reveal three-dimensional flow phenomena and separation characteristics

DOI: 10.54254/2755-2721/2026.KA31247

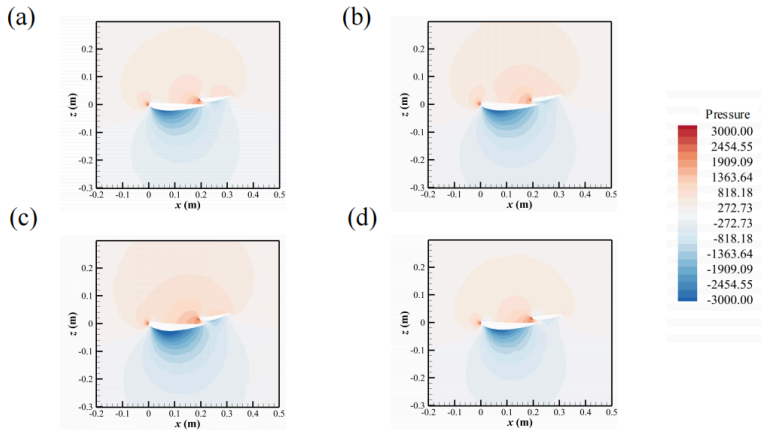

Figure 16. Static pressure contours in the mid-plane: (a) Case S1, (b) Case S2, (c) Case S3, and (d) Case S4. The slot-jet interaction and wake development are visualized through pressure distribution

3.4. Experimental validation and the effect of the angle of attack

Wind tunnel experiments were carried out to validate the computational predictions, using the optimal configuration identified from the first-stage DoE and CFD analysis (Case F1). The experimentally measured lift-to-drag ratio was 12.43, which compares favorably with the CFD prediction of 10.06. The modest difference is likely due to the distinct flow velocities employed in the two approaches: the wind tunnel tests were conducted at a maximum velocity of 12.6 m/s, whereas the CFD simulations assumed 73 m/s. Despite this disparity, the close agreement between the two approaches provides strong support for the reliability of the simulation methodology.

Beyond validation at the design condition, the wind tunnel study also examined the effect of incidence on aerodynamic performance. Tests were performed at five angles of attack: 0 °, 5 °, 10 °, 15 °, and 20 °. The corresponding lift-to-drag ratios were 12.43, 7.03, 6.18, 4.29, and 3.15, respectively. These measurements reveal a monotonic decline in aerodynamic efficiency with increasing angle of attack. The trend is consistent with the progressive onset of flow separation and the associated rise in pressure drag at higher incidence. Thus, the experimental investigation not only substantiates the numerical results at the design condition, but also provides useful insight into the off-design behavior of the optimized wing configuration.

Table 8. Experimentally measured lift-to-drag ratios at different angles of attack

Angle of attack (°)	L/D
0	12.43
5	7.03
10	6.18
15	4.29
20	3.15

DOI: 10.54254/2755-2721/2026.KA31247

Table 9. Comparison of experimental and CFD results for Case 1 at 0.00◦ angle of attack

Parameter	CFD	Experiment
Velocity (m/s)	73.0	12.6
Lift-to-drag ratio (L/D)	10.06	12.43

4. Concluding remarks and future directions

This study has investigated the aerodynamics of dual-element rear wings through an integrated program of theoretical analysis, computational fluid dynamics (CFD), design of experiments (DoE), and wind-tunnel testing. A two-stage Taguchi design approach efficiently identified the geometric parameters that maximize the lift-to-drag ratio while maintaining significant downforce.

The theoretical framework describes the main principles of multi-element wing aerodynamics and provides a physical explanation for the observed performance trends. CFD analyses show that the optimal configuration (Case S4) achieves high aerodynamic efficiency through a combination of pressure recovery, controlled boundary-layer development, and reduced vortex-induced losses. Experimental measurements generally agree with the CFD results, with lift-to-drag ratios closely matching despite differences in Reynolds number.

From this study, several conclusions can be drawn. The relative angle between wing elements appears to be the most influential factor for aerodynamic efficiency, while camber distribution affects the balance between downforce and drag. Moderate camber values (around 4%) provide a reasonable compromise between generating sufficient downforce and limiting drag.

This study shows four refined rear-wing profiles obtained from the second-stage Taguchi optimization as a complete aerodynamic package. Each profile has a lift-to-drag ratio above 10, with the most efficient one (Case S4) reaching 11.88. Even the least efficient design (Case S3, with a lift-to-drag ratio of 10.03) may still be useful in practice, especially on low-speed circuits, as it produces the highest downforce of 816.91 N.

Although this study provides an understanding of dual-element rear-wing aerodynamics, there are opportunities for future work. Additional factors could be investigated, such as a wider variety of airfoil profiles with different camber, thickness, concavity radius, or flap-element concavity. The design space could also be extended to include endplates, adjustable flap mechanisms like Drag Reduction Systems (DRS), and Gurney flaps. Exploring these elements would help develop a more complete performance map and support further optimization for high-performance applications.

References

[1] M. Simmons, “How fast is an F1 car compared to IndyCar, WEC, super formula and more, ” Autosport, 2022, Accessed: Aug. 24, 2025. [Online]. Available: https: //www.autosport.com/general/news/solving-the-race-series-comparison-question/9460507/

[2] Formula 1, “Everything you need to know about F1 – drivers, teams, cars, circuits and more.” 2025. Accessed: Aug. 24, 2025. [Online]. Available: https: //www.formula1.com/en/latest/article/drivers-teams-cars-circuits-and-more-everything-you-need-to-know-about.7iQfL3Rivf1comzdqV5jwc

[3] R. Braybrook, “What are the fastest and slowest corners on the F1 calendar?” Motorsport.com, 2024, Accessed: Aug. 24, 2025. [Online]. Available: https: //www.motorsport.com/f1/news/fastest-slowest-turns-f1-calendar/10572266/

[4] U. photographer, “Ferrari formula 1 car in motion.” https: //www.publicdomainpictures.net/en/view-image.php?image=299455& picture=charles-leclerc-f1.

DOI: 10.54254/2755-2721/2026.KA31247

[5] E. Benini, R. Campiglia, and P. Stagnaro, “Multi-objective optimization of slot-geometry for a multi-element airfoil, ” Journal of Aircraft, vol. 48, no. 4, pp. 1262–1269, 2011, doi: 10.2514/1.C031233.
[6] J. Zhang and I. P. Zerihan, “Aeroelastic and aerodynamic ground-effect studies on a slotted wing in high planform loading, ” AIAA Journal, vol. 41, no. 8, pp. 1587–1595, 2003, doi: 10.2514/2.2057.
[7] I. M. Roberts, R. Sutton, and A. A. Kiejna, “Cornering effects on inverted multi-element wings in ground effect, ” Proc. IMechE Part G: Journal of Aerospace Engineering, vol. 223, no. 6, pp. 745–755, 2009, doi: 10.1243/09544100JAERO61.
[8] K. H. Jung, K. Taira, and Y. Tamayama, “Influence of endplate clearance on tip-vortex behavior and induced drag, ” Chinese Journal of Aeronautics, vol. 26, no. 5, pp. 1067–1073, 2013, doi: 10.1016/S1000-9361(13)60183-5.
[9] C. A. B. Monteiro, “Numerical study of a drag reduction system for a formula student car, ” Master’s thesis, Universidade NOVA de Lisboa (Portugal), 2021.
[10] F. Mendes, F. Martins, and R. de Oliveira, “Analysis of drag reduction system effects on multi-element wing performance, ” Vehicles, vol. 4, no. 9, pp. 1–16, 2022, doi: 10.3390/vehicles4090309.
[11] C. L. Rumsey et al., “Summary of the x-30 and 30P30N multi-element airfoil experiments, ” NASA Langley Research Center, NASA TM-2014-218021, 2014. Available: https: //ntrs.nasa.gov/api/citations/20160006011/downloads/20160006011.pdf
[12] A. M. Rayhan, M. S. Hossain, R. H. Mim, and M. Ali, “Computational and experimental study on the aerodynamic performance of NACA 4412 airfoil with slot and groove, ” Heliyon, vol. 10, no. 11, p. e31595, 2024, doi: https: //doi.org/10.1016/j.heliyon.2024.e31595.
[13] A. Choudhry, M. Baig, M. Hafeez, M. Feroz, M. Younis, and Q. Rasool, “Computational analysis of high lift generating airfoils for small wind turbine applications, ” Wind Energy Science Discussions, pp. 1–25, 2020, doi: 10.5194/wes-2020-14.
[14] U. A. C. Database, “NACA 4412 airfoil data.” http: //airfoiltools.com/airfoil/details?airfoil=naca4412-il.
[15] B. Erdoğan and G. Taşkaya, “Optimization of NACA 6412 using taguchi method and computational fluid dynamics analysis, ” Sustainability, vol. 17, no. 13, 2025, doi: 10.3390/su17135861.
[16] U. A. C. Database, “NACA 6412 airfoil data.” http: //airfoiltools.com/airfoil/details?airfoil=naca6412-il.
[17] M. S. Selig and J. Guglielmo, “High-lift low reynolds number airfoil design, ” Journal of Aircraft, vol. 34, no. 1, pp. 72–79, 1997, doi: 10.2514/2.2188.
[18] U. A. C. Database, “S1223 airfoil data.” http: //airfoiltools.com/airfoil/details?airfoil=s1223-il.
[19] U. A. C. Database, “Eppler E423 airfoil data.” http: //airfoiltools.com/airfoil/details?airfoil=e423-il.
[20] S. Chandra and R. Tyagi, “Study of eppler 423 airfoil with gurney flap and vortex generators, ” Advances in Aerospace Science and Technology, vol. 5, pp. 1–19, Jan. 2020, doi: 10.4236/aast.2020.51001.
[21] Prof. D. A. Piyush chavda, “An aerodynamics analysis of rear wing of formula–1 car using eppler E423 as wing profile, ” International Journal of Research in Advent Technology, 2018, Available: https: //www.ijrat.org/downloads/Vol-6/dec-2018/Paper%20ID-612201840.pdf
[22] F. A. Administration, Airplane flying handbook (FAA-h-8083-3A). 2004. Available: https: //www.faa.gov/sites/faa.gov/files/regulations_policies/handbooks_manuals/aviation/airplane_handbook/06_afh_ch5.pdf
[23] L. W. Hunton, “Effects of twist and camber on the low-speed characteristics of a large-scale swept-back wing, ” NACA, RM A50A10, 1950. Available: https: //ntrs.nasa.gov/api/citations/19930086645/downloads/19930086645.pdf
[24] A. M. O. Smith, “High-lift aerodynamics, ” NASA, NASA TM-19960054343, 1996. Available: https: //ntrs.nasa.gov/api/citations/19960054343/downloads/19960054343.pdf
[25] B. W. Pomeroy and M. S. Selig, “Design of airfoils to mitigate wake bursting, ” in AIAA aviation forum, 2017. Available: https: //m-selig.ae.illinois.edu/pubs/PomeroySelig-2017-AIAA-2017-1210-Design-for-WakeBursting.pdf
[26] S. Hosseini, “Airframe technologies to enable future efficient transports.” Presentation at German Aerospace Center (DLR), Braunschweig, 2023. Available: https: //ntrs.nasa.gov/api/citations/20230013557/downloads/DLR_visit_Hosseini_Charts_9_15_22.pdf
[27] B. R. Hiller, R. L. Campbell, and M. N. Lynde, “Design exploration of a slotted-wing common research model, ” NASA Langley Research Center, Technical Report, 2021. Available: https: //ntrs.nasa.gov/api/citations/20205002835/downloads/Hiller2021.pdf
[28] Fédération Internationale de l’Automobile, “2020 italian grand prix – final qualifying classification, ” FIA, 2020. Available: https: //www.fia.com/sites/default/files/doc_36_-_2020_italian_grand_prix_-_final_qualifying_classification.pdf